GeoHealth

RESEARCH ARTICLE
10.1029/2024GH001114

Key Points:

- Ground urban heat island (GUHI) is proposed to improve satellite thermal observations applied for heat risk management
- GUHIs are warmer and show complex spatial contrasts with surface urban heat islands
- Urban materials and structures contribute differently to diurnal dynamics of GUHIs

Supporting Information:

Supporting Information may be found in the online version of this article.

Correspondence to:

L. Hu,
lh0063@uah.edu

Citation:

Hu, L., & Uejio, C. (2024). Ground urban heat island: Strengthening the connection between Spaceborne thermal observations and urban heat risk management. *GeoHealth*, *8*, e2024GH001114. https://doi.org/10.1029/2024GH001114

Received 17 MAY 2024
Accepted 17 JUL 2024

Author Contributions:

Conceptualization: Leiqiu Hu
Data curation: Leiqiu Hu
Formal analysis: Leiqiu Hu
Funding acquisition: Leiqiu Hu, Christopher Uejio
Investigation: Leiqiu Hu
Methodology: Leiqiu Hu
Project administration: Christopher Uejio
Resources: Leiqiu Hu
Visualization: Leiqiu Hu
Writing – original draft: Leiqiu Hu
Writing – review & editing: Christopher Uejio

Ground Urban Heat Island: Strengthening the Connection Between Spaceborne Thermal Observations and Urban Heat Risk Management

Leiqiu Hu[1] **and Christopher Uejio**[2]

[1]University of Alabama in Huntsville, Huntsville, AL, USA, [2]Florida State University, Tallahassee, FL, USA

Abstract As urbanization progresses under a changing climate, urban populations face increasing threats from chronically higher heat exposures and more frequent extreme heat events. Understanding the complex urban thermal exposure patterns becomes crucial for effective heat risk management. The spatial advantage of satellite thermal observations positions surface urban heat islands (SUHI) as a primary measure for such applications at the city scale. However, satellite-inherent biases pose considerable uncertainties. To improve the representation of human-relevant heat exposure, this study proposes a simple but effective satellite-based measure– ground urban heat island (GUHI), focusing solely on radiant temperatures from urban ground elements. Leveraging ECOSTRESS land surface temperature product and radiation-based statistical downscaling, diurnally representative GUHIs were evaluated over NYC. The findings reveal that overall GUHI is consistently warmer than SUHI diurnally. However, GUHI exhibits complex spatial contrasts with SUHI, primarily influenced by vegetation coverage. Various indicators associated with urban structures and materials were examined, showing important but dissimilar roles in shaping the spatial dynamics of GUHI and SUHI. This study highlights the value of satellite thermal observations compared to air temperature while addressing uncertainties in widely adopted practices of using them. By improving the depiction of human-related urban heat patterns from Earth observations, this research offers valuable insight and more reliable measures to address the urgent requirements for urban heat risk management globally.

Plain Language Summary As cities grow under a changing climate, people in urban areas face more heat, putting them at risk. To protect them, it's crucial to understand where and when heat is most intense in cities. Direct satellite measurements help show surface urban heat islands (SUHI) that are widely used for mapping hot spots to identify higher heat risks and vulnerable communities. However, this method can be biased. This study suggests a new way to measure heat in cities using satellites that only consider the heat coming from the ground in urban areas, called ground urban heat islands (GUHI). By using data from the ECOSTRESS aboard the International Space Station and statistical approaches, we looked at how hot urban ground was throughout the day in New York City. We found that overall, GUHI was consistently hotter than SUHI throughout the day. However, heat patterns depicted by GUHI were influenced by urban surface properties in complex ways and were often different from SUHI at the local scale. This research shows that using satellite data to measure heat can give us better insights than air temperature for spatial applications, and this study offers more reliable ways to support heat risk management in cities worldwide.

1. Introduction

Nowadays, more than half of the global population lives in built environments (United Nations, 2018). As urbanization continues, urban populations face increasing threats from chronic high summer heat exposure due to urban heat island effects, as well as more frequent and severe extreme heat events in the context of global warming (Oleson et al., 2015; Wu et al., 2023). Understanding the complex heat patterns within the metropolitan area is often the first step required for planning and decision-making related to heat adaptation and mitigation for negative heat-related outcomes in public health, urban ecosystems, energy, and other sectors.

Satellite-based land surface temperature (LST) has become dominant in urban heat island (UHI) and heat-related vulnerability/risk studies, due to its accessibility and the fast-growing volume of thermal products at various frequencies and spatial resolutions. Importantly, the instantaneous scan over a relatively large spatial domain offers significant spatial advantages to capture the rather complex temperature structure over heterogeneous urban landscapes, compared with traditional sparse ground weather stations (for measurements of air

temperature). Despite the growing number of dense urban observational networks and emerging crowd-sourced air temperature observations (Johnson et al., 2020; Potgieter et al., 2021; Schatz & Kucharik, 2016), their applications for urban heat management, and other relevant climate services are constrained by data availability, accessibility, and quality. Thus, satellite-based LST maps are considered the primary or one of the few heat data sources to guide heat mitigations and adaptations in many cities (Keith et al., 2019) as well as to assess thermal equity (Benz & Burney, 2021; Hsu et al., 2021) despite that limited evidence has been established or supports the direct LST applications for health risks at the city-regional scales (Dousset et al., 2011; Wolff et al., 2021). Canopy layer UHI, measured by air temperature, has distinguishable spatiotemporal patterns compared to remotely sensed UHI using LST, also known as the surface urban heat island (SUHI), particularly during the daytime. For example, a recent study suggests insufficient capacity from satellite observations for municipal heat mitigation at an actionable scale (Turner et al., 2022). The majority of widely-accepted thermal comfort or heat exposure metrics, particularly for health risk, in the literature are built on air temperature, or a collection of several biometeorological variables measured at the screen height (1.2–2 m above the ground) (Bobb et al., 2014; Sailor et al., 2016).

Satellite remote sensing using a fixed field of view (FOV) faces inherent challenges over heterogeneous surfaces, complicating the interpretation of LST applied over urban areas. On the one hand, the directional variation over 3D structured surfaces is predominant for wide FOV sensors (Hu et al., 2016; Lagouarde & Irvine, 2008; Voogt & Oke, 2003). Voogt and Oke (1997) proposed using complete surface temperature (T_c) that accounts for all active surfaces, including walls, ground, and roofs of buildings, as well as urban greenery over urban landscapes, to overcome thermal anisotropy effects in thermal observations for urban climate studies. However, T_c is not directly observable from satellites. A handful of studies on this topic have relied on either process-based model simulations to fully resolve all surface temperatures without vegetation, particularly trees (Hall et al., 2024; Jiang et al., 2017; Yang et al., 2020), or a combination of airborne and ground-based observations (Voogt & Oke, 1997). Neither approach is practical for long-term or large-scale applications.

On the other hand, thermal anisotropy becomes less significant for observations from narrow FOV sensors, but simply using direct bird's-eye-view observations over heterogeneous and rough urban surfaces often remains questionable when dealing with thermal comfort and heat-exposure outcomes related to the health of the urban ecosystem and urban residents (Martilli et al., 2020). For example, these 2D projected LSTs observed from space over 3D urban surfaces are biased toward a considerable fraction of roofs and treetops (Roth et al., 1989; Stewart et al., 2021). For example, the building-to-plan ratio (percentage of the lot area that is covered by buildings) in Brooklyn neighborhoods, New York City (NYC) is about 45%, and blocks in Manhattan can easily reach more than 50% (Hu & Wendel, 2019). Urban residents' outdoor activities occur at the ground level, where wall and ground surface temperatures are more relevant due to radiative energy exchanges near the ground for both long-wave and short-wave radiation. In other words, thermal observations that do not resolve and/or distinguish ground conditions can be biased for heat management applications for pedestrians and outdoor workers (Vanos et al., 2016). Additionally, there is a tradeoff between spatial resolution and revisit frequency in satellite thermal products, largely limiting their meaningful applications in cities featured with distinctly diurnal and seasonal thermal patterns. Despite the dramatic increase in Earth observation-based urban heat studies, current applications, particularly focused on spatial comparisons, remain relatively disconnected from the particular needs for human-relevant urban thermal environment research (Stewart et al., 2021).

To address some of the aforementioned gaps, this study proposes a new measurement of heat from Earth observation–ground-level urban heat island (GUHI), which accounts for the thermal conditions at the bottom of urban canyons. Using NYC as an example, we illustrate a pathway to estimate representative city-scale ground-level LST (LST_{Ground}) at a fine resolution (70 m in this case) based on LST from ECOsystem Spaceborne Thermal Radiometer Experiment on Space Station (ECOSTRESS) product. Assessment of GUHI's spatial and diurnal dynamics provides a basic understanding of their characteristics. The direct comparison between GUHI and SUHI (using original pixel LST, or LST_{Pixel}) is also performed for the first time to offer a quantitative understanding of uncertainties associated with using SUHI for intra-urban heat-related applications. Finally, the study identifies sensitive factors that influence GUHI as well as these contributing to the contrasts between LST_{Ground} and LST_{Pixel}. The study aims to share new insights into a more relevant concept and feasible means of using thermal remote sensing to address the pressing needs of sustainable development in cities facing increased heat challenges.

2. LST and Thermal Comfort

The outdoor urban thermal environment is highly heterogeneous due to the interplay of several biometeorological components, such as radiation, wind speed, temperature, and humidity. All of these variables are strongly influenced by cross-scale urban structures and functions (Höppe, 1999; Jendritzky et al., 2012; Lindberg et al., 2016), resulting in complex patterns that are challenging to observe or model. Some field studies suggest that the spatial variability of air temperature does not effectively capture the spatial patterns of heat load on pedestrians (Mayer et al., 2008; Middel & Krayenhoff, 2019). Part of the reason is that the turbulent mixing of free-moving air dampens the spatial contrasts. Additionally, ambient radiation is an important element of the full heat load experienced by outdoor pedestrians, with a disproportionately higher influence when solar radiation is strong. Mean radiant temperature (MRT) is a common term used to quantify the ambient long-wave and short-wave radiation on thermal comfort (Guo et al., 2020; Lindberg et al., 2016; Middel & Krayenhoff, 2019; Middel et al., 2021). Reanalyzing microclimate-scale observations from the MaRTy system by Middel and Krayenhoff (2019) in Tempe, Arizona, illustrates an equivalent or mostly superior predictability of LST_{Ground} compared to the widely-adopted proxy–air temperature, for spatial patterns of thermal comfort metrics, namely, MRT, Physiologically Equivalent Temperature (PET) (Höppe, 1999; Matzarakis et al., 1999), and Universal Thermal Climate Index (UTCI) (Jendritzky et al., 2012) (see R^2 and ρ in Figure 1). The latter two indices are widely used to quantify thermal physiological stress, accounting for the collective effects of air temperature, wind speed, humidity, and radiation through heat balance and physiological models. On one hand, it is noted that although air temperature and surface temperature are modulated by some common energy transport processes, these two quantities are fundamentally different: one is thermodynamic equilibrium status of air flow and another one is radiometric term estimated from thermal radiance (Norman & Becker, 1995). Thus, as shown in Figure 1, the dynamic range of air temperature (39.3–48.5°C) is much smaller than LST_{Ground} (30.0–65.8°C). LST_{Ground} quantitatively matches MRT and PET better, showing lower coefficients of variation (CV), especially during the hottest hours, but shows larger differences with UTCI in terms of absolute values than air temperature. On the other hand, given the strong contribution of radiation to heat stress, it is not surprising that diurnal LST_{Ground} is more sensitive to distinguish the spatial variation of heat load compared to ambient air temperature (see Figure 1). This holds true for PET and UTCI during the hottest hours of the day when stress peaks. For example, the partial correlation coefficient between LST_{Ground} and PET (UTCI) at the local hottest hour reaches up to 0.81 (0.77), whereas air temperature only shows a correlation of 0.48 (0.49). Collectively, LST_{Ground} better captures spatial variations in human heat exposure and thermal comfort compared to air temperature.

The thermal stress imposed on pedestrians originates from the 3D ambient environments. The MaRTy study in Tempe, AZ also suggests a dominant contribution from lateral radiation on six-direction-weighted MRT, particularly from the long-wave portion, followed by surface imperviousness (Middel & Krayenhoff, 2019). On one hand, within the complex street structures, buildings cast shadows on the canyon floor, reducing the short-wave radiant heat load on pedestrians. On the other hand, the "cavity" effects on both long-wave and short-wave radiation, by inducing multiple reflections, absorptions, and re-emissions, consequently promote energy exchanges among all active vertical facades and floors. These effects also modify the short-term dynamics of heat load within the street canyon. The morphology of the canyon structure and materials, as well as street orientation, are major factors that control ambient radiant contributions to heat load, exhibiting considerable spatial diversity across a city. From this perspective, although LST_{Ground} is a direct measurement of outgoing long-wave radiation, the value is also considered a result of the energy balance among radiatively active surfaces within the canyon. This partly explains the stronger spatial agreement from LST_{Ground} for MRT than air temperature (see Figure 1), despite not directly accounting for short-wave radiation.

Besides the Tempe example at touch-scale or person-scale observations, LST_{Ground} can be better associated with street-level heat exposure or thermal comfort at the neighborhood scale across a city, which most satellite thermal observations can capture. Town Energy Model (TEB) (Masson, 2000) is used to resolve streetscape facade surface temperatures over NYC neighborhoods with various canyon structures, the aspect ratios of which range from 0.34 to 4.09 (equivalent to ground sky view factor (SVF) from 0.99 to 0.44). The simulations account for two perpendicular streets with orientations at 38°and 128°, and trees or grassland are not considered in the street canyon. The detailed model setup and simulations are described in Hu and Wendel (2019). Figure 2 summarizes the absolute differences of diurnal street canyon surface temperatures. Overall, LST_{Ground} agrees very well with LST_{Walls} at night (Figure 2b) but are persistently warmer than the roof during nighttime hours (lateral and vertical long-wave radiation) (Figure 2a). Much warmer daytime ground surfaces compared with walls can dominate the

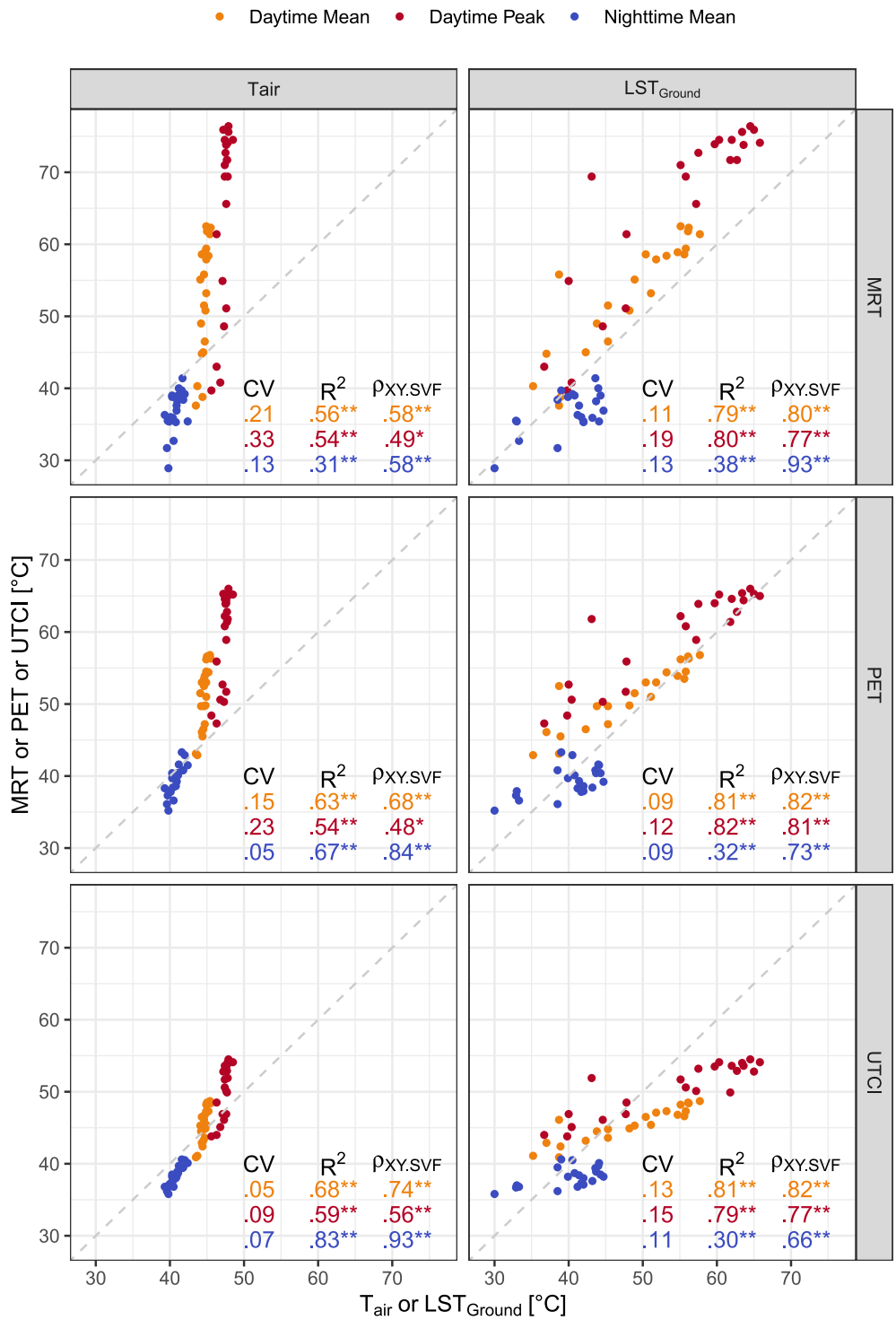

Figure 1. Comparison of pedestrian-level thermal exposure using ambient air temperature (T_{air}) and ground radiant temperature (also as LST_{Ground}) against the mean radiant temperature (MRT), physiologically equivalent temperature (PET), and universal thermal climate index. *CV* is coefficient of variation which is calculated by the ratio of the root mean squared error (RMSE) to the mean of the variable. R^2 refers to the coefficient of determination. $\rho_{XY.SVF}$ is the partial correlation coefficient between X (T_{air} or LST_{Ground}) and Y (MRT or PET) with a given sampled sky view factor controlled. * is denoted for $p < 0.05$ and ** for $p < 0.01$. The measurements are from Table 3 in Middel and Krayenhoff (2019), which summarized observations measured by the mobile human-biometeorological station over 22 sites in Tempe, Arizona.

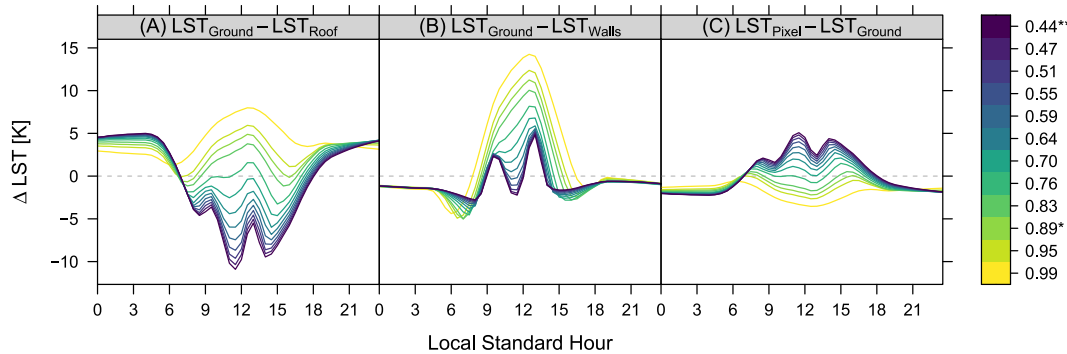

Figure 2. Averaged hourly surface temperature differences between street-canyon ground and building roofs (a), ground and building walls (b), as well as simulated entire scene and ground (c). The TEB simulations at various ground SVFs with two street directions (38° and 128°) were compared under the clear-sky conditions during Map-Sept. The simulated scene has a building-to-plan ratio of 0.45. The emissivities of roofs and roads are assumed at 0.97 and 0.96, respectively. * denotes the ground sky view factor for typical Brooklyn neighborhoods and ** for blocks in Manhattan.

radiation contributions to heat loads. These explain both higher daytime and nighttime correlations between hyper-local MRT with LST_{Ground} (Figure 1b).

Figure 2c demonstrates considerable time-dependent contrasts between LST_{Ground} and LST_{Pixel} at the neighborhood scale. The nocturnal disparities among urban element temperatures suggest an underestimation of thermal heat load using LST_{Pixel}, despite the differences being relatively small among different street morphologies. The daytime thermal disparities are much larger and more sensitive to canyon geometries. Shallower street canyons (e.g., wide roads with low-rise buildings) exhibit greater temperature differences when the solar elevation angle is relatively high (near noon). In such scenarios, elevated short-wave radiation increases the heat load on pedestrians, and warmer LST_{Ground} can better capture such exposure. For a deeper canyon structure, shade from buildings relieves the shortwave radiation impact, and LST_{Pixel} often overestimates the heat load by considering much higher roof temperatures from tall buildings. It is worth mentioning that the largest $\Delta LST_{Pixel-Ground}$ is about 8.4 K at 11:30 a.m., which is close to the overpass time of Sun-synchronous orbiters (such as Terra and Landsat). Furthermore, the simulation scenarios are idealized and do not account for the roles of vegetation and water bodies. The actual differences between LST_{Ground} and LST_{Pixel} can be much more complex both diurnally and spatially.

3. Material and Methods

3.1. LST_{Ground} Estimation

To better assess the diurnal and spatial variability of GUHI using LST_{Ground} for potential applications in intra-urban heat exposure research, this study considers the recent high-resolution diurnally-representative LST product from ECOSTRESS aboard the International Space Station. ECOSTRESS is in a lower Earth orbit, unlike sun-synchronous orbits, providing more frequent (1–5 days) revisits at different times of day. The level-2 LST products are derived from a multi-band temperature and emissivity separation retrieval algorithm similar to the Advanced Spaceborne Thermal Emission and Reflection Radiometer (ASTER)'s retrieval algorithm (Hulley & Hook, 2018), which improves emissivity estimations, particularly over complex urban landscapes, resulting in generally better LST retrievals (Hulley et al., 2022). Here, clear-sky ECOSTRESS LST imagery (resampled at 70 m resolution) during the growing season (May-September, 2018–2021) over New York City was collected. Necessary preprocessing was conducted, including additional cloud screening and cloud masking, and georeferencing, yielding a total of 35 clear-sky LST images for later analyses (see the list in Table S1 of Supporting Information S1).

Here, we consider LST_{Ground} that accounts for the urban elements at the ground level, excluding roofs, tree canopies, and other elements above the ground. To achieve that, the idea is to estimate sub-pixel urban element temperatures and then reconstruct the LST based solely on ground elements. The downscaling processes for sub-pixel temperatures rely on linear unmixing of long-wave radiation collectively contributed by thermal emittance from various urban landscape elements within a given pixel. A convolutional model using a 5-by-5 focal moving

window (25 pixels with a domain of 350 m by 350 m) is applied to statistically identify optimal solutions for up to eight unknown end-member temperatures, with predefined temperature bounding constraints for each type. This approach assumes that the surface materials and morphological characteristics of each urban land element are similar at a (sub)neighborhood scale, represented by a 5- by five-pixel focus window. Consequently, the associated surface temperatures for each land cover type are comparable within the focal domain. The fractions of urban elements at each 70 m pixel are estimated from a high-resolution land cover map (2017, 0.15 m, derived from LiDAR and ortho-imagery), including soil (1.2% of the total NYC domain), building roofs (14.4%), roads (9.9%), general imperviousness (17.4%, such as parking lots, sidewalks, etc.), tree canopies (16.0%), grassland (11.8%), and water surfaces (28.8%, including rivers and bays within the domain). It's important to note that the street-orientation-induced ground-level temperature differences are not distinguished in the statistical approach. Therefore, the solved ground-level temperature of a given type is considered a spatial mean under various illumination conditions at the neighborhood scale. Using the convolutional analysis structure, element temperature estimates within each given pixel involve other neighboring 24 pixels, helping to reduce uncertainties in statistical solutions and control the potential impact of random errors. Details on handling downscaling are described in the Supporting Information S1 Section of *Radiance-based Endmember Unmixing*.

Next, the sub-pixel urban element radiations are re-aggregated at the original pixel scale, but only accounting for long-wave radiation from ground-level elements, including roads, general imperviousness, and grassland. Due to the scattered and low coverage of soil (1.2%) and railway (0.5%) in the NYC domain, these two ground covers are not considered in LST_{Ground} estimates. Water surfaces are excluded as most human activities occur on land. The downscaling scheme is realized on the statistical fitting; thus, errors are inevitable. To fairly compare the ground-level estimates with pixel-level LSTs across the city, LST_{Pixel} is recalculated based on all considered urban land elements (ground elements as well as building roofs and tree canopies). Here, only urban land pixels are considered for analyses, including those with partial water surfaces (about 3.3% of the total pixels). All pure water pixels (28.8% of the entire domain) are masked for domain-wide comparisons. There is a very small fraction of pure urban land pixels (0.0%–0.3%) over the NYC domain.

3.2. Attribution Analyses

To understand what and how factors influence the spatial patterns of GUHI and to discern the primary drivers contributing to the divergence between GUHI and SUHI, we employed a series of generalized additive models (GAMs) (Wood, 2011, 2017). These models were used to establish the statistical relations between spatial variations of a temperature pattern and various relevant urban surface properties. Equation 1 represents the generic form of the model for any given pattern of y (e.g., LST_{Ground}, LST_{Pixel}, or $LST_{Pixel-Ground}$) at time t, where R_{btp} indicates the building-to-plan ratio, R_{tree} for tree coverage ratio, R_{grass} for grass coverage ratio, R_{imp} for ground imperviousness ratio, $H_{building}$ for mean building height in meter, $Hsd_{building}$ for the building height variation ($[m]$), and ρ_{roof} for roof reflectance in percent, along with additional control factor, such as distance to water bodies (D_{water} $[m]$, less than 1 km) due to their widespread distribution in NYC and strong thermal influences. Roof reflectance estimation is described in the Supporting Information S1. The model accounts for individual terms (s function) as well as the marginal interactive effects of two or more variables (ti function) in thin plate regression splines (nonlinearly) (Wood, 2006). The model fitting is determined by the fast restricted maximum likelihood (REML) method (Wood, 2011).

$$\begin{aligned} y_t = {} & a_t + s(R_{btp}) + s(R_{imp}) + s(R_{grass}) + s(R_{tree}) + s(\rho_{roof}) + \\ & s(H_{building}) + s(Hstd_{building}) + s(Dist_{water}) + s(x,y) + \\ & ti(R_{tree},R_{grass}) + ti(R_{totalimperviousness},R_{grass}) + \\ & ti(H_{building},Hstd_{building},\rho_{roof}) + s(x,y) + \epsilon_t \end{aligned} \tag{1}$$

where a_t and ϵ_t indicate the intercept and error at the time t, respectively. The model is applied to spatial maps of LST_{Ground}, LST_{Pixel}, and $LST_{Pixel-Ground}$ at each sampled time. The model performances, assessed using adjusted R^2, are illustrated in Figure S4 of Supporting Information S1. Generally, static surface features considered in the model better capture spatial variation of LST_{Pixel} compared to LST_{Ground}. The relatively low adjusted R^2 in the case of $LST_{Pixel-Ground}$ indicates more complex effects that cannot be effectively explained by the selected variables and their interactions.

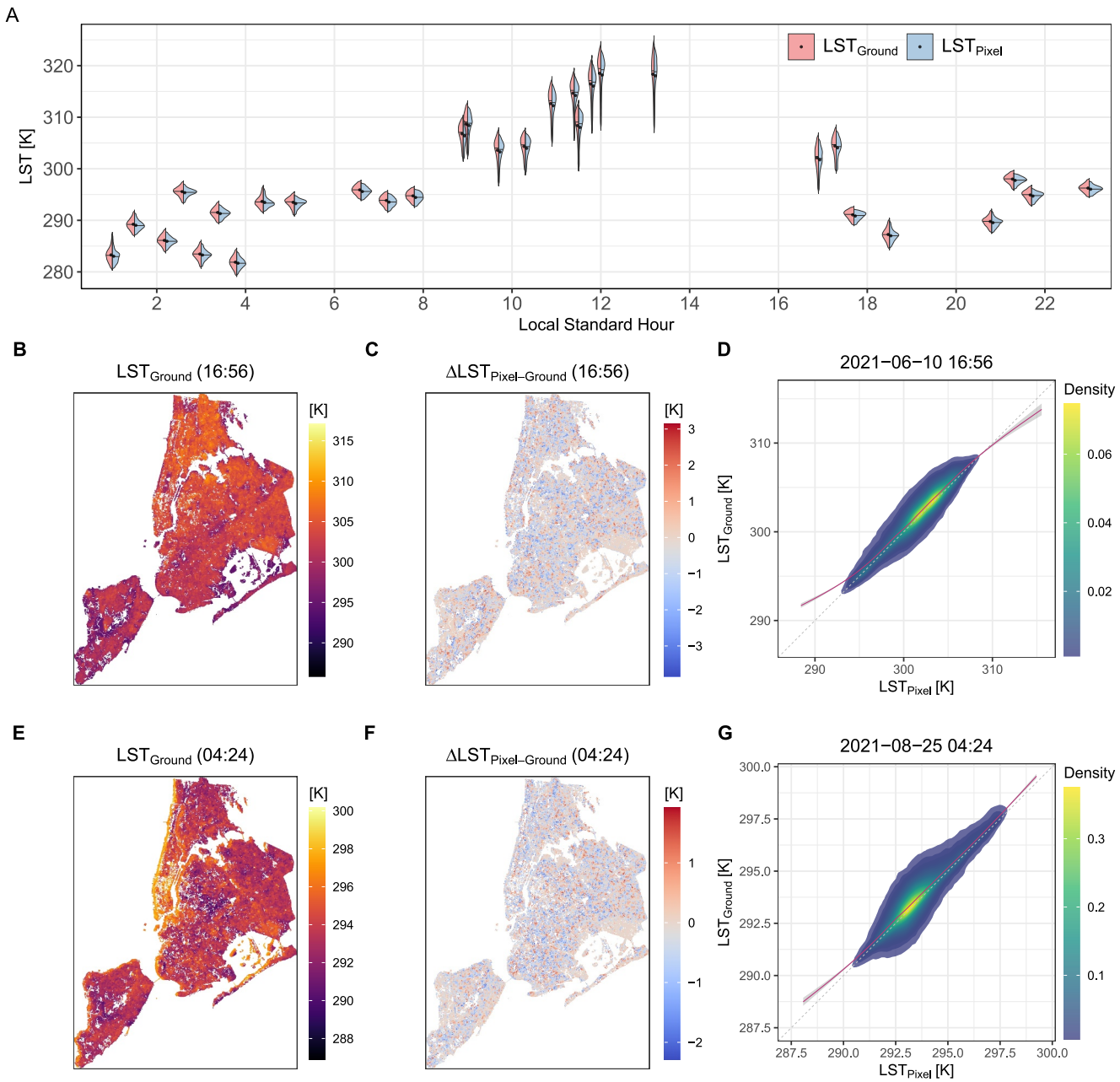

Figure 3. (a) Density distributions of ground-level (red) and pixel-level (blue) land surface temperature over NYC diurnally, displaying only 5%–95% quantiles for better visual effects. The urban domain median and mean are represented by bars and dots, respectively. Examples of daytime (b) (16:56 local time on 10-06-2021) and nighttime (e) (at 04:24 local time on 25-08-2021) LST_{Ground} maps. Panels (c and f) illustrate the spatial differences between LST_{Ground} and LST_{Pixel} estimates, displaying values within 4 times of interquartile range for a better visual effect. Panels (d and g) are density scatter plots comparing LST_{Pixel} and LST_{Ground}, with their nonlinear fitting lines shown in red. See Figure S2 in Supporting Information S1 for a near-noon example map on 03-08-2020 at 13:12 as well as Figure S3 in Supporting Information S1 for comparisons of the fitted lines among all sampled hours.

4. Results

4.1. Temporal and Spatial Patterns of GUHI

The diurnal change of GUHI is similar to SUHI but generally exhibits larger intra-urban spatial variations with slightly higher mean temperatures (Figure 3a). Note that due to the images being sampled from different days under various meteorological conditions (e.g., T_{air}), the results from different hours are not directly comparable. Therefore, we focus on the comparison of each pair of GUHI and SUHI. The warmer daytime LSTs peak around

noon to early afternoon among the sampled times, exhibiting a generally much greater daytime variation than the nighttime patterns. City-wide LST_{Ground} is 0.41–0.58 K (0.40–0.72 K) warmer on average (median) than LST_{Pixel} but there are no statistically significant differences between day and night. Figures 3b and 3e show a pair of day and night GUHI and their spatial differences with the corresponding SUHI results (Figures 3c and 3f). The overall GUHI patterns mostly resemble typical patterns observed in SUHI, showing statistically significant spatial correlation coefficients ranging from 0.73 to 0.91 (see Figure S1 in Supporting Information S1). For instance, Manhattan exhibits warmer temperature for both day and night than other boroughs. However, significant contrasts are evident at the local scale, showing a rather random salt-and-pepper pattern in their differences. Figures 3d and 3e, and Figure S3 in Supporting Information S1 for all analyzed hours unveil interesting relationships between LST_{Ground} and LST_{Pixel}. For example, daytime LST_{Ground} tends to be cooler than LST_{Pixel} over the hottest regions, while they are disproportionately warmer over the cooler regions in NYC. The tendency of cooler LST_{Ground} at warmer regions is also observed at nighttime, albeit with a much weaker contrast and less prevalence compared to their daytime signals. Collectively, the presence of both heterogeneous local contrasts and similar temperature-dependent disparities suggests influences not only from highly variable local-scale surface materials and structures but also from similar urban forms at a larger urban landscape scale (e.g., Manhattan vs. Staten Island).

4.2. Drivers for Intra-Urban Variations of GUHI

Taking a closer look at compositions of common urban landscape elements and their associated temperatures in Figure 4a, city-scale mean roof temperature is the highest in the late morning to early afternoon hours, followed by human-made ground surfaces. Meanwhile, tree canopies are often warmer than the grassland around the hottest hours. These elevated urban components receive more direct solar radiation and are less prone to shadows. During the daytime, the mean temperatures of roads and impervious ground are similar and considerably higher than grassland which is the coolest component on average. Roofs and tree canopies have shown accelerated cooling compared to ground-level components since late evening, attributed to often larger view factors. Throughout the night, human-made ground surfaces remain the warmest components on average, while grassland becomes slightly warmer than tree canopies. These overall patterns agree with observations from the field and airborne campaigns (Morrison et al., 2018, 2021; Wetherley et al., 2018).

Furthermore, Figure 4b illustrates the probability distributions of differences between two major urban elements, emphasizing the local contrast of LST between ground-level elements and those above ground. Building roofs are generally considered warmer during the day (up to 0.10 K on average compared to roads and impervious surfaces over the domain) and cooler at night (up to 0.68–0.78 K on average). However, the local variation of relative differences between roofs and ground imperviousness (including roads) is considerable, following a normal distribution with a stronger daytime variation across the city. Similar diurnal local-difference distributions are observed between tree canopies and grassland, with a smaller contrast compared to human-made surfaces. Overall, these distributions highlight that local properties, such as thermal and geometric properties, can vary the relative temperatures of urban components in highly heterogeneous urban settings. On the other hand, mean differences across the city follow general expectations, showing cooler roof and tree canopy temperatures at night compared to human-made and vegetative ground surfaces on average. Counterintuitively, city-wide local $LSTs_{Ground}$ are warmer than their corresponding pixel-level values around noon (up to 0.4 K difference on average), even though roofs and tree canopies on average tend to be warmer than their ground counterparts at the same time. The local contrasts of ground and LST_{Pixel}s have a negatively skewed distribution. A considerable proportion of pixels show small differences between ground and pixel LST diurnally, but it is also common to observe much warmer $LSTs_{Ground}$ than their pixel-level counterparts, partly owing to local heterogeneity and pixel-level urban compositions. For example, sparse low-rise industrial areas typically featured with white roofs may have warmer ground temperatures. Additionally, the water influences in the partial water pixels also contribute to a lower LST_{Pixel} during the daytime, which is excluded in LST_{Ground} estimates directly. The overall pixel-ground LST differences ($LST_{Pixel-Ground}$) have a smaller variation (ranging from −0.40– − 0.16 K on the city average) compared to the contrasts found among the urban components (i.e., roofs-roads: (−0.68, 0.10), roof-imperviousness: (−0.78, 0.02), trees-grass: (−0.61, 0.06) in K).

The spatial variability of GUHI is significantly influenced by building density (building-to-plan ratio) (Figure 5a) and mean building height (Figure 5e), exhibiting distinct diurnal controls. A marked increase in LST_{Ground} over high-density building districts is evident during hours with high solar angles (around noon), contributing up to

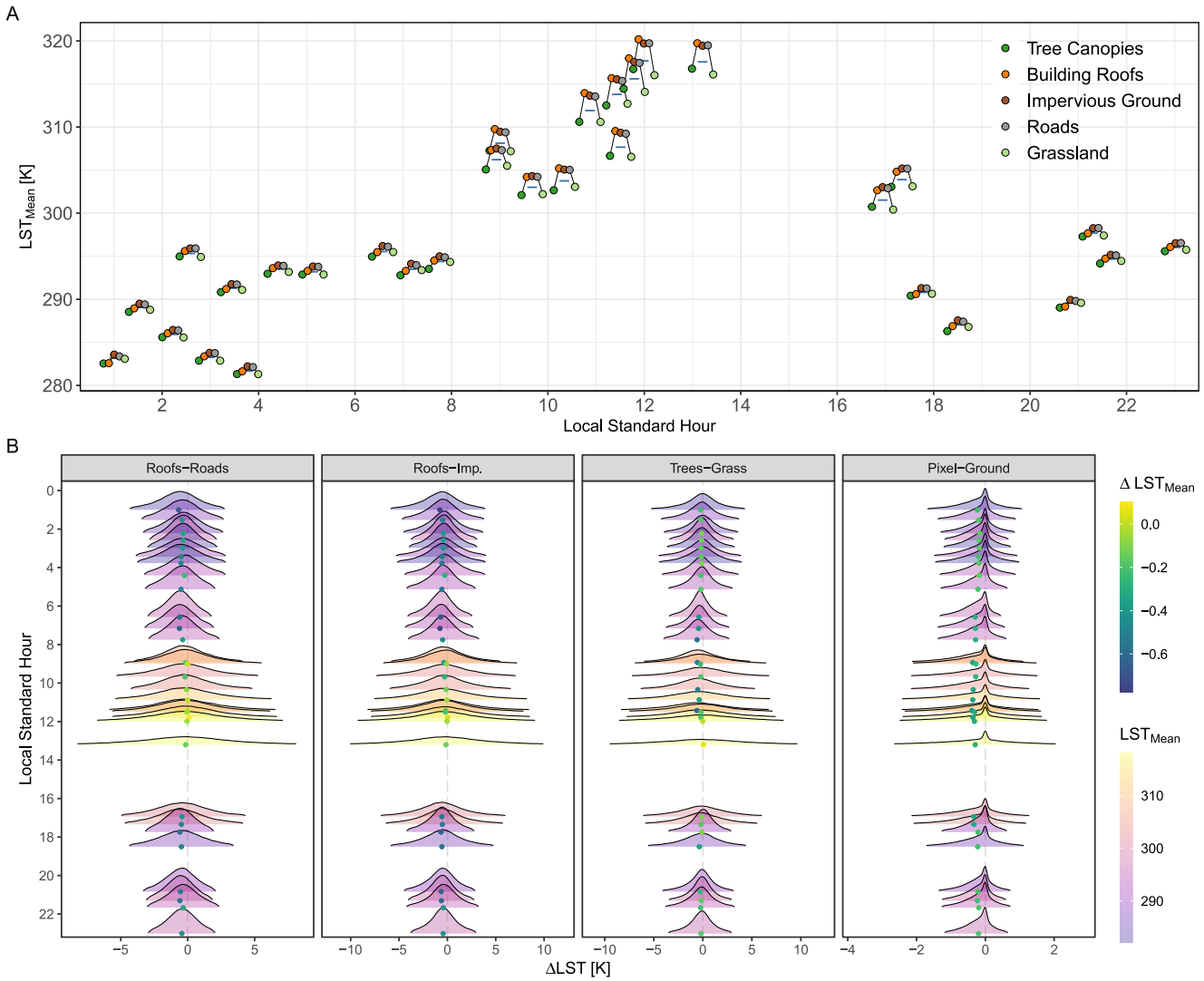

Figure 4. (a) City-scale mean temperatures of five major urban elements estimated at the subpixel level. The dots represent domain-mean LSTs (K) of different urban elements, and the horizontal bars indicate the mean land surface temperature of the entire NYC domain at each sampled time. (b) Density distribution of pixel-level differences between two urban components. The 1%–99% quantiles of urban element temperature differences are summarized in each probability density distribution, and their colors correspond to the domain mean LSTs. The dots represent the domain mean values of each distribution, with their magnitudes indicated by different colors.

2.2 K to the spatial change, while its nighttime effects are generally opposite but considerably weaker (up to 0.5 K). The heating and cooling of the ground around noon are influenced by enhanced radiation absorption via multi-reflections in highly convoluted street canyons and a higher chance of shadows over compactly built areas. Statistical results suggest that the radiative geometry of the canyon (trapping effect) outweighs the shading effect (Song & Wang, 2015) during summer daytime hours, along with wind shelter effects by decreasing turbulent sensible heat loss, and other potential processes such as elevated anthropogenic emissions. As expected, building density exhibits a more pronounced influence on LST_{Pixel} around noon (Figure S5a in Supporting Information S1, up to 4.4 K) due to minimized shading at roofs. Additionally, in areas with taller buildings at a given density, the chance of shadows on the ground increases, naturally resulting in a lower ground temperature (Figure 5e). Nocturnal cooling of urban ground is slowed by trapping effects and other processes (such as wind) over tall building districts, resulting in higher LST_{Ground} (up to 0.9 K), although the ground of compact areas generally accumulates less total radiation during daylight hours (lower LST_{Ground} up to 1.0 K). The impervious area ratio exhibits a predominantly positive relationship with LST_{Ground}, showing linearity during nighttime hours and peaking around 75% coverage during the day. These relationships also hold true for LST_{Pixel} (see Figures S5e and

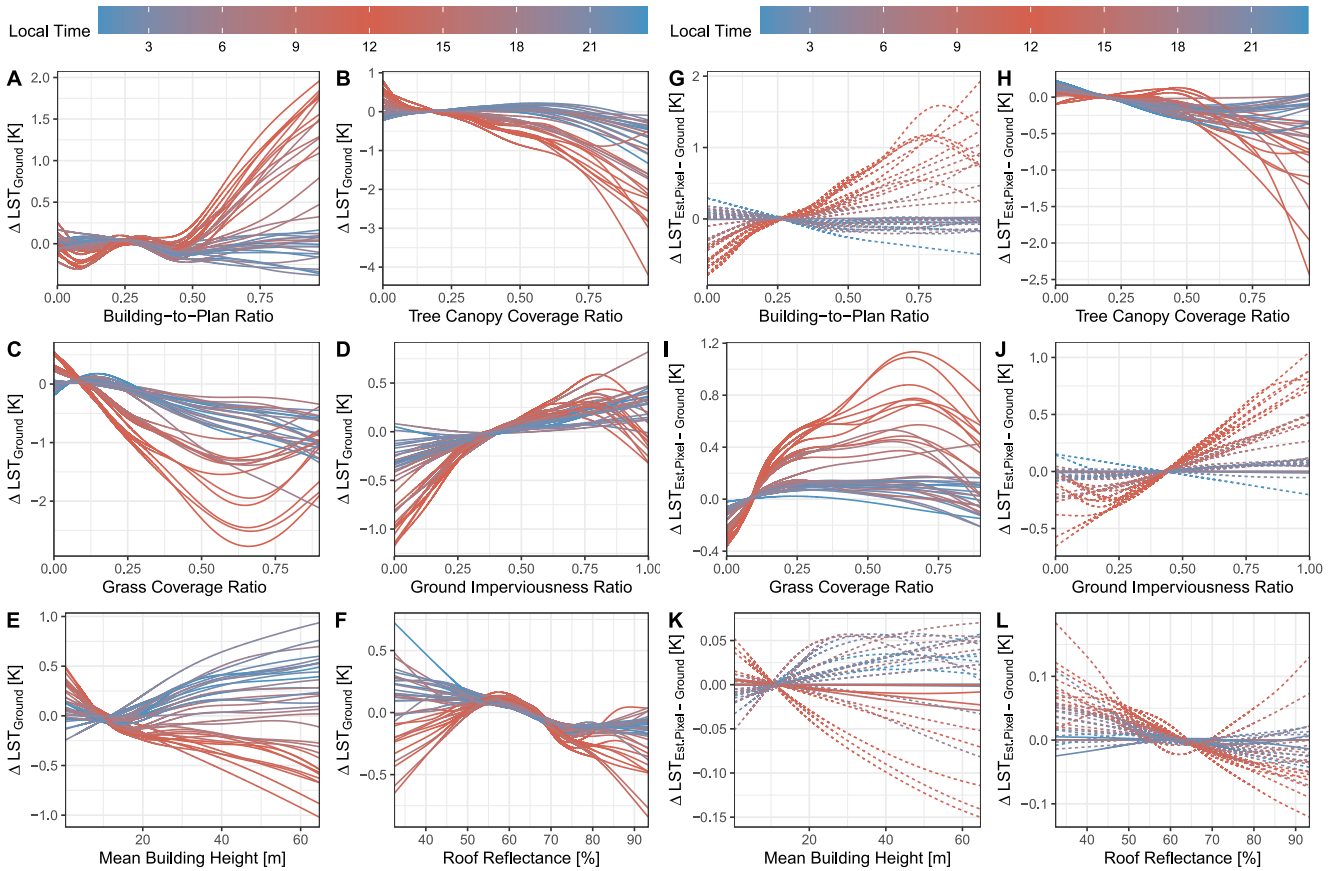

Figure 5. GAM analysis results showing the diurnal relationship between the spatial variations of LST_{Ground} (a–f) and $LST_{Pixel-Ground}$ (g–l) with surface material-related and morphological features. Solid lines indicate statistically significant results at $p = 0.05$ significance level, dashed lines for p-value at 0.1 level, and insignificant results are not shown. The 0%–99% quantile of mean heights (e and k) is displayed. Building height standard deviation results are presented in Figure S6 of Supporting Information S1.

S5d in Supporting Information S1), with a considerably stronger impact during daytime hours. Furthermore, roof reflectance is mostly negatively correlated with LST_{Ground} statistically, as expected, with a weaker effect at nighttime. A nonsymmetric single-peak pattern is detected during daytime hours, but note the possible uncertainties of roof reflectance underestimation due to shadows (see details in Supporting Information S1). Overall, these human-made surface materials and structures (namely, building height, density, impervious ground coverage, and roof reflectance) influence both surface temperatures significantly, but they do not provide statistically significant (p at 0.05) explanations for the differences in pixel and ground-level LSTs (Figures 5g, 5j, 5k and 5l).

On the other hand, non-built components, including both ground-level grass and shrubs and above-ground tree canopies, exert significant influences on LST_{Ground} (refer to Figures 5b and 5c). This influence follows a similar pattern, where an increased coverage of tree canopies or surface greenness typically results in lower ground temperatures throughout the day. However, the processes governing their effects differ. For instance, tree canopies directly lower ground temperature through shading and indirectly through reducing ambient temperature via increased latent heat flux partitioning (Hu & Li, 2020; Johnson et al., 2020; Ziter et al., 2019). Conversely, cooler grassland, considered part of the urban ground surface, results in a direct lowering of LST_{Ground} (refer to Figure 4a).

The contrast between LST_{Ground} and LST_{Pixel} spatially is primarily driven by the coverage of vegetation components, identified as the only statistically significant factors among all analyzed terms (see Figures 5h and 5i). On one hand, vegetation coverage exhibits a substantially higher impact on $\Delta LST_{Pixel-Ground}$ during the daytime (up to 2.6 K for trees and 1.5 K for grass) compared to nighttime (up to 0.7 K for trees, and 0.3 K for grass). An evident

cooling effect on daytime LST_{Pixel} is observed when tree canopies dominate within the pixel (Figure S5b in Supporting Information S1), displaying a mostly linear relationship. The effects of trees on LST_{Ground} primarily result from two competing processes (trapping and shading effects) that strongly depend on their coverage. Consequently, there is a slow decrease in LST_{Ground} when tree coverage is low, followed by a relatively accelerated decrease when tree canopies become predominant during the daytime hours (Figure 5b). The contrasting effects collectively contribute to an overall nonlinear role of tree canopies in differentiating LST_{Ground} and LST_{Pixel}. Equally interesting is the daytime influence of grassland coverage on both temperatures, particularly when grassland is dominant (Figure 5c and Figure S5c in Supporting Information S1). The nonlinear relationship during the hottest hours as a function of grassland coverage is likely associated with the relative openness of the grassland. Larger grassland areas (high coverage ratio) are more likely to be exposed to direct sunlight around noon, which could lead to relatively warmer ground and pixel temperatures compared to smaller ones near buildings and/or trees. However, overall, grassland contributes to daytime cooling in LST_{Ground} but has a relatively weaker cooling on LST_{Pixel} based on its coverage during daytime hours. As a result, Figure 5i suggests a robust and nonlinear role of grassland in explaining daytime $LST_{Pixel-Ground}$. On the other hand, tree canopy coverage differentiates the nocturnal pixel and ground temperatures, but its impact is much weaker than during the daytime. In contrast, grassland coverage shows little nocturnal influence on $\Delta LST_{Pixel-Ground}$.

Besides the analyzed static surface features in terms of their coverages, soil moisture also affects the physiological conditions of urban greenery and thus their surface temperatures, which further modifies the spatial variation of LST_{Ground}. For example, Figure S7 in Supporting Information S1 compares six images obtained at similar local times (10:52–11:59) but featuring different lengths of drying periods from prior precipitation events. Despite trees having an overall stronger control on both temperatures compared to grassland around 11 a.m., grassland appears to be more sensitive to large soil moisture changes (14 drying days vs. others). However, this sensitivity is less clear when the soil moisture change is less significant or with a shorter drying period (1–5 days). Additionally, soil moisture's impact on surface cooling becomes more pronounced when the coverages of trees and grassland become more dominant.

5. Discussion and Conclusions

LST_{Pixel} is the primary observational source for spatial applications of SUHIs. Many studies, focusing on topics like environmental justice, heat vulnerability, and heat mitigation, heavily rely on LST_{Pixel} analysis directly from various satellite products. Given the complexity and heterogeneous nature of built environments, and the inherent limitations of satellite remote sensing systems, such as the tradeoff of spatial and temporal resolutions and thermal anisotropy caused by inconsistent viewing angles (Hu et al., 2016; Voogt & Oke, 1998; Wang et al., 2022), uncertainties arising from the use of direct satellite observations over urban areas can accumulate. These restrict meaningful spatial comparisons of LST for urban heat applications. This study proposed a new concept of urban heat island measures from EO—GUHI, which spatially better captures heat exposures at the neighborhood scale. Using the most recent fine-resolution ECOSTRESS LST product, the study offers a feasible way to quantify the diurnal dynamics of GUHIs. Further comparisons between the new GUHI and traditional SUHIs also provide valuable insights into understanding the uncertainties of using LST_{Pixel} and facilitate the interpretation of existing results from the literature with meaningful context.

Figures 3c and 3e shows the rather random distributions of $\Delta LST_{Pixel-Ground}$ at ECOSTRESS pixel scale, and Figure 4b illustrates differences vary diurnally, reaching their maximal spatial variation around hottest hours. As most applications for health and community disparities linked with socioeconomic status are often conducted at neighborhood (or US census tracts) and postal mailing code levels, Figures 6b–6e summarizes the aggregated surface temperature contrasts at these scales for daytime and nighttime. This comparison confirms that the spatial aggregation yields a lower level of uncertainties (contrast between ground and pixel LSTs). In other words, for large scale comparison, the spatial variation of LST_{Pixel} remains reasonable. However, the noticeable local differences also present heterogeneously. Clearly, due to some diverging diurnal forcing from urban surface properties, the spatial uncertainties are not consistent over time (see Figure S8 in Supporting Information S1). For example, the warm biased daytime LST_{Pixel} (relative to LST_{Ground}) can have a cold bias at nighttime. Thus, further cautions should be noted while interpreting the LST_{Pixel}-based spatial results for day and night separately. Of course, estimation of LST_{Ground} requires considerable resources, particularly representative fine-resolution land cover and land use map, which is not universally available for many metropolitan areas. Still, in cities with

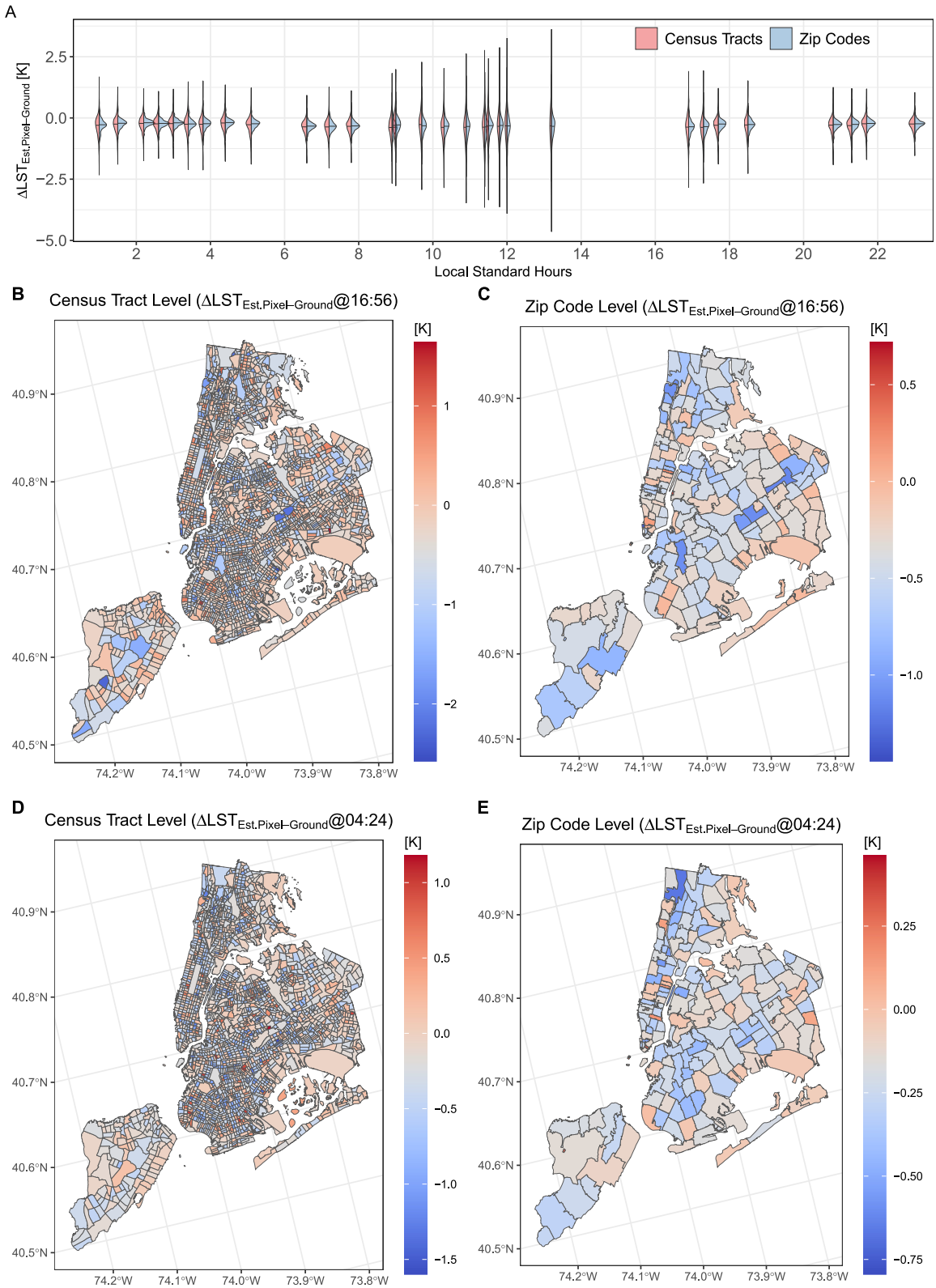

Figure 6. Temperature differences between GUHI and SUHI applications at census tracts and zip code levels. (a) Illustrates the diurnal distributions for 30 out of 35 analyzed images at two scales. (b–c) showcase daytime spatial patterns (16:56) of the land surface temperature differences at Census Tracts and Zip Codes. (d–e) display nighttime patterns at 4:24. Outliers (extreme values), detected based on 3 times of interquartile range, have been excluded for illustration purposes.

available high-resolution land cover products and thermal observations, researchers should consider GUHI for decision-making support.

Understanding GUHI is achieved through the statistical downscaling process in this study, which relies on representative higher-resolution land cover information and geospatially aligned thermal observations. Uncertainties in LST_{Ground} estimation stem from various factors, particular attention is required when applying this concept across different domains using diverse Earth observations. For instance, errors in thermal observation retrieval are inevitable and can impact LST_{Ground}. Wide-view-angle thermal observations may exacerbate errors due to misrepresentation of surface features typically observed from off-nadir viewpoints, including urban vertical surfaces (Hu & Wendel, 2019). The spatial resolution of LST and the relative homogeneity of the urban landscape determine the statistical robustness and physical meaningfulness of downscaling, which is related to the assumption regarding neighboring pixels used to calculate sub-pixel urban element temperatures. The application should align the data choice with the nature of the urban landscape. Finally, the statistically estimated LST_{Ground} represents the neighborhood-scale mean result at a given sensor viewing angle. It is noted that estimated LST_{Ground} underrepresents ground surfaces under the trees, which are not seen by the sensor due to the blockage of tree canopies. The actual ground temperature can also differ due to various shading/illumination conditions influenced by building morphologies and street orientations. Importantly, EO-based LST_{Ground} represents the relative thermal disparities at the neighborhood scale and should not be interpreted for individual heat exposure at street level.

Similar to SUHIs that show considerable global variations (Peng et al., 2012) and are strongly influenced by background biomes, geography (Imhoff et al., 2010), as well as urban forms and functions (Zhou et al., 2019), GUHI is expected to vary globally driven by similar features, albeit with varying degrees of influences. The NYC case reveals that urban structures, namely building heights and density, and urban materials, including vegetation coverage and roof albedo, play statistically significant roles in modulating spatial variations of both GUHI and SUHI diurnally, except for building height variability (see Figure S6 in Supporting Information S1), which is only significant for SUHI (p at 0.05). However, considerable differences in their influence levels are also observed (see Figure 5a vs. Figure S5a in Supporting Information S1; Figure 5c vs. Figure S5c in Supporting Information S1). Overall, the larger spatial variations with warmer temperatures of GUHI exemplified using one of the world's most populous cities have meaningful and important implications for thermal comfort and heat exposure applications using satellite thermal observations.

Conflict of Interest

The authors declare no conflicts of interest relevant to this study.

Data Availability Statement

All data and software used are publicly accessible. ECOSTRESS Level 2 LST product is downloaded from NASA apρEEARS (https://appeears.earthdatacloud.nasa.gov/). The high-resolution land cover data (raster) are from openNYC portal (https://data.cityofnewyork.us/Environment/Land-Cover-Raster-Data-2017-6in-Resolution/he6d-2qns). Building footprints and heights (vector, attribution table) are from the same portal (https://data.cityofnewyork.us/Housing-Development/Building-Heights/pffy-49n3). The NAIP data in 2015 and 2017 used for roof reflectance are accessed via Earth Explorer (https://earthexplorer.usgs.gov/). TEB model V3 (Surfex8.1) is open source and available via https://opensource.umr-cnrm.fr/projects/teb/files.

Acknowledgments
This research is supported by NASA's Health and Air Quality Science Team (80NSSC21K0430), NASA ECOSTRESS Science and Application Team (80NSSC23K0306), and NASA Interdisciplinary Research in Earth Science (IDS) (80NSSC20K1263).

References

Benz, S. A., & Burney, J. A. (2021). Widespread race and class disparities in surface urban heat extremes across the United States. *Earth's Future*, *9*(7), 1–14. https://doi.org/10.1029/2021EF002016

Bobb, J. F., Peng, R. D., Bell, M. L., & Dominici, F. (2014). Heat-related mortality and adaptation to heat in the United States. *Environmental Health Perspectives*, *122*(8), 811–816. https://doi.org/10.1289/ehp.1307392

Dousset, B., Gourmelon, F., Laaidi, K., Zeghnoun, A., Giraudet, E., Bretin, P., et al. (2011). Satellite monitoring of summer heat waves in the Paris metropolitan area. *International Journal of Climatology*, *31*(2), 313–323. https://doi.org/10.1002/joc.2222

Guo, H., Aviv, D., Loyola, M., Teitelbaum, E., Houchois, N., & Meggers, F. (2020). On the understanding of the mean radiant temperature within both the indoor and outdoor environment, a critical review. *Renewable & Sustainable Energy Reviews*, *117*, 109207. https://doi.org/10.1016/j.rser.2019.06.014

Hall, T. W., Blunn, L., Grimmond, S., McCarroll, N., Merchant, C. J., Morrison, W., et al. (2024). Utility of thermal remote sensing for evaluation of a high-resolution weather model in a city. *Quarterly Journal of the Royal Meteorological Society*, *150*(760), 1771–1790. https://doi.org/10.1002/qj.4669

Höppe, P. (1999). The physiological equivalent temperature—A universal index for the biometeorological assessment of the thermal environment. *International Journal of Biometeorology*, *43*(2), 71–75. https://doi.org/10.1007/s004840050118

Hsu, A., Sheriff, G., Chakraborty, T., & Manya, D. (2021). Disproportionate exposure to urban heat island intensity across major US cities. *Nature Communications*, *12*(1), 2721. https://doi.org/10.1038/s41467-021-22799-5

Hu, L., & Li, Q. (2020). Greenspace, Bluespace, and their interactive influence on urban thermal environments. *Environmental Research Letters*, *15*(3), 034041. https://doi.org/10.1088/1748-9326/ab6c30

Hu, L., Monaghan, A., Voogt, J. A., & Barlage, M. (2016). A first satellite-based observational assessment of urban thermal anisotropy. *Remote Sensing of Environment*, *181*, 111–121. https://doi.org/10.1016/j.rse.2016.03.043

Hu, L., & Wendel, J. (2019). Analysis of urban surface morphologic effects on diurnal thermal directional anisotropy. *ISPRS Journal of Photogrammetry and Remote Sensing*, *148*, 1–12. https://doi.org/10.1016/j.isprsjprs.2018.12.004

Hulley, G. C., Göttsche, F. M., Rivera, G., Hook, S. J., Freepartner, R. J., Martin, M. A., et al. (2022). Validation and quality assessment of the ECOSTRESS level-2 land surface temperature and emissivity product. *IEEE Transactions on Geoscience and Remote Sensing*, *60*, 1–23. https://doi.org/10.1109/tgrs.2021.3079879

Hulley, G. C., & Hook, S. J. (2018). ECOSTRESS level-2 LST and emissivity ATBD (Tech. Rep.).

Imhoff, M. L., Zhang, P., Wolfe, R. E., & Bounoua, L. (2010). Remote sensing of the urban heat island effect across biomes in the continental USA. *Remote Sensing of Environment*, *114*(3), 504–513. https://doi.org/10.1016/j.rse.2009.10.008

Jendritzky, G., de Dear, R., & Havenith, G. (2012). UTCI—Why another thermal index? *International Journal of Biometeorology*, *56*(3), 421–428. https://doi.org/10.1007/s00484-011-0513-7

Jiang, L., Zhan, W., & Zou, Z. (2017). Two methods for remote estimation of complete urban surface temperature. *The International Archives of the Photogrammetry, Remote Sensing and Spatial Information Sciences*, *42*, 479–487. https://doi.org/10.5194/isprs-archives-XLII-2-W7-479-2017

Johnson, S., Ross, Z., Kheirbek, I., & Ito, K. (2020). Characterization of intra-urban spatial variation in observed summer ambient temperature from the New York City community air survey. *Urban Climate*, *31*(March 2019), 100583. https://doi.org/10.1016/j.uclim.2020.100583

Keith, L., Meerow, S., & Wagner, T. (2019). Planning for extreme heat: A review. *Journal of Extreme Events*, *06*(03n04), 2050003. https://doi.org/10.1142/s2345737620500037

Lagouarde, J.-P., & Irvine, M. (2008). Directional anisotropy in thermal infrared measurements over Toulouse city centre during the Capitoul measurement campaigns: First results. *Meteorology and Atmospheric Physics*, *102*(3–4), 173–185. https://doi.org/10.1007/s00703-008-0325-4

Lindberg, F., Onomura, S., & Grimmond, C. S. B. (2016). Influence of ground surface characteristics on the mean radiant temperature in urban areas. *International Journal of Biometeorology*, *60*(9), 1439–1452. https://doi.org/10.1007/s00484-016-1135-x

Martilli, A., Krayenhoff, E. S., & Nazarian, N. (2020). Is the urban heat island intensity relevant for heat mitigation studies? *Urban Climate*, *31*, 100541. https://doi.org/10.1016/j.uclim.2019.100541

Masson, V. (2000). A physically-based scheme for the urban energy budget in atmospheric models. *Boundary-Layer Meteorology*, *94*(3), 357–397. https://doi.org/10.1023/A:1002463829265

Matzarakis, A., Mayer, H., & Iziomon, M. (1999). Applications of a universal thermal index: Physiological equivalent temperature. *International Journal of Biometeorology*, *43*(2), 76–84. https://doi.org/10.1007/s004840050119

Mayer, H., Holst, J., Dostal, P., Imbery, F., & Schindler, D. (2008). Human thermal comfort in summer within an urban street canyon in central Europe. *Meteorologische Zeitschrift*, *17*(3), 241–250. https://doi.org/10.1127/0941-2948/2008/0285

Middel, A., Alkhaled, S., Schneider, F. A., Hagen, B., & Coseo, P. (2021). 50 grades of shade. *Bulletin of the American Meteorological Society*, *102*(9), 1–35. https://doi.org/10.1175/bams-d-20-0193.1

Middel, A., & Krayenhoff, E. S. (2019). Micrometeorological determinants of pedestrian thermal exposure during record-breaking heat in Tempe, Arizona: Introducing the MaRTy observational platform. *Science of the Total Environment*, *687*, 137–151. https://doi.org/10.1016/j.scitotenv.2019.06.085

Morrison, W., Kotthaus, S., Grimmond, C. S. B., Inagaki, A., Yin, T., Gastellu-Etchegorry, J.-P., et al. (2018). A novel method to obtain three-dimensional urban surface temperature from ground-based thermography. *Remote Sensing of Environment*, *215*, 268–283. https://doi.org/10.1016/J.RSE.2018.05.004

Morrison, W., Kotthaus, S., & Grimmond, S. (2021). Urban surface temperature observations from ground-based thermography: Intra- and inter-facet variability. *Urban Climate*, *35*(December 2020), 100748. https://doi.org/10.1016/j.uclim.2020.100748

Norman, J. M., & Becker, F. (1995). Terminology in thermal infrared remote sensing of natural surfaces. *Agricultural and Forest Meteorology*, *77*(3–4), 153–166. https://doi.org/10.1016/0168-1923(95)02259-Z

Oleson, K. W., Monaghan, A., Wilhelmi, O., Barlage, M., Brunsell, N., Feddema, J., et al. (2015). Interactions between urbanization, heat stress, and climate change. *Climate Change*, *129*(3–4), 525–541. https://doi.org/10.1007/s10584-013-0936-8

Peng, S., Piao, S., Ciais, P., Friedlingstein, P., Ottle, C., Bréon, F.-M., et al. (2012). Surface urban heat island across 419 global big cities. *Environmental Science and Technology*, *46*(2), 696–703. https://doi.org/10.1021/es2030438

Potgieter, J., Nazarian, N., Lipson, M. J., Hart, M. A., Ulpiani, G., Morrison, W., & Benjamin, K. (2021). Combining high-resolution land use data with crowdsourced air temperature to investigate intra-urban microclimate. *Frontiers in Environmental Science*, *9*, 1–19. https://doi.org/10.3389/fenvs.2021.720323

Roth, M., Oke, T. R., & Emery, W. J. (1989). Satellite-derived urban heat islands from three coastal cities and the utilization of such data in urban climatology. *International Journal of Remote Sensing*, *10*(11), 1699–1720. https://doi.org/10.1080/01431168908904002

Sailor, D., Shepherd, M., Sheridan, S., Stone, B., Kalkstein, L., Russell, A., et al. (2016). Improving heat-related health outcomes in an urban environment with science-based policy. *Sustainability: Science, Practice and Policy*, *8*(10), 1015. https://doi.org/10.3390/su8101015

Schatz, J., & Kucharik, C. J. (2016). Urban heat island effects on growing seasons and heating and cooling degree days in Madison, Wisconsin USA. *International Journal of Climatology*, *36*(15), 4873–4884. https://doi.org/10.1002/joc.4675

Song, J., & Wang, Z.-H. (2015). Interfacing the urban Land–Atmosphere system through coupled urban canopy and atmospheric models. *Bound.-Layer Meteorol.*, *154*(3), 427–448. https://doi.org/10.1007/s10546-014-9980-9

Stewart, I. D., Krayenhoff, E. S., Voogt, J. A., Lachapelle, J. A., Allen, M. A., & Broadbent, A. M. (2021). Time evolution of the surface urban heat island. *Earth's Future*, *9*(10), e2021EF002178. https://doi.org/10.1029/2021EF002178

Turner, K., Rogers, M. L., Zhang, Y., Middel, A., Schneider, F. A., Ocón, J. P., et al. (2022). More than surface temperature: Mitigating thermal exposure in hyper-local land system. *Journal of Land Use Science*, *17*(1), 79–99. https://doi.org/10.1080/1747423X.2021.2015003

United Nations. (2018). *The World's cities in 2018 (Tech. Rep.)*. United Nations.

Vanos, J. K., Middel, A., McKercher, G. R., Kuras, E. R., & Ruddell, B. L. (2016). Hot playgrounds and children's health: A multiscale analysis of surface temperatures in Arizona, USA. *Landscape and Urban Planning*, *146*, 29–42. https://doi.org/10.1016/j.landurbplan.2015.10.007

Voogt, J. A., & Oke, T. R. (1997). Complete urban surface temperatures. *Journal of Applied Meteorology*, *36*(9), 1117–1132. https://doi.org/10.1175/1520-0450(1997)036⟨1117:CUST⟩2.0.CO;2

Voogt, J. A., & Oke, T. R. (1998). Effects of urban surface geometry on remotely-sensed surface temperature. *International Journal of Remote Sensing*, *19*(5), 895–921. https://doi.org/10.1080/014311698215784

Voogt, J. A., & Oke, T. R. (2003). Thermal remote sensing of urban climates. *Remote Sensing of Environment*, *86*(3), 370–384. https://doi.org/10.1016/S0034-4257(03)00079-8

Wang, D., Chen, Y., Hu, L., Voogt, J. A., & He, X. (2022). Satellite-based daytime urban thermal anisotropy: A comparison of 25 global cities. *Remote Sensing of Environment*, *283*, 113312. https://doi.org/10.1016/j.rse.2022.113312

Wetherley, E. B., McFadden, J. P., & Roberts, D. A. (2018). Megacity-scale analysis of urban vegetation temperatures. *Remote Sensing of Environment*, *213*, 18–33. https://doi.org/10.1016/J.RSE.2018.04.051

Wolff, N. H., Zeppetello, L. R. V., Parsons, L. A., Aggraeni, I., Battisti, D. S., Ebi, K. L., et al. (2021). The effect of deforestation and climate change on all-cause mortality and unsafe work conditions due to heat exposure in Berau, Indonesia: A modelling study. *The Lancet Planetary Health*, *5*(12), e882–e892. https://doi.org/10.1016/S2542-5196(21)00279-5

Wood, S. N. (2006). Low-Rank Scale-Invariant tensor product smooths for generalized additive mixed models. *Biometrics*, *62*(4), 1025–1036. https://doi.org/10.1111/j.1541-0420.2006.00574.x

Wood, S. N. (2011). Fast stable restricted maximum likelihood and marginal likelihood estimation of semiparametric generalized linear models. *Journal of the Royal Statistical Society. Series B Stat. Methodol.*, *73*(1), 3–36. https://doi.org/10.1111/j.1467-9868.2010.00749.x

Wood, S. N. (2017). *Generalized additive models*. Chapman and Hall/CRC. https://doi.org/10.1201/9781315370279

Wu, H., Su, X., & Singh, V. P. (2023). Increasing risks of future compound climate extremes with warming over global land Masses. *Earth's Future*, *11*(9), e2022EF003466. https://doi.org/10.1029/2022ef003466

Yang, J., Wong, M. S., Ho, H. C., Krayenhoff, E. S., Chan, P., Abbas, S., & Menenti, M. (2020). A semi-empirical method for estimating complete surface temperature from radiometric surface temperature, a study in Hong Kong city. *Remote Sensing of Environment*, *237*, 111540. https://doi.org/10.1016/j.rse.2019.111540

Zhou, D., Xiao, J., Bonafoni, S., Berger, C., Deilami, K., Zhou, Y., et al. (2019). Satellite remote sensing of surface urban heat islands: Progress, challenges, and perspectives. *Remote Sensing*, *11*(1), 48. https://doi.org/10.3390/rs11010048

Ziter, C. D., Pedersen, E. J., Kucharik, C. J., & Turner, M. G. (2019). Scale-dependent interactions between tree canopy cover and impervious surfaces reduce daytime urban heat during summer. *Proceedings of the National Academy of Sciences*, *116*(15), 7575–7580. https://doi.org/10.1073/pnas.1817561116